The Astronomical Journal, 167:117 (15pp), 2024 March https://doi.org/10.3847/1538-3881/ad1ff6

Observations with the Differential Speckle Survey Instrument. XI. First Year of Observations from Apache Point Observatory

James W. Davidson, Jr.[1], Elliott P. Horch[2,7], Steven R. Majewski[1], Evan Fagan[1], Melissa A. Shea[2], Torrie Sutherland[2], Robert F. Wilson[3], D. Xavier Lesley[2,8], Richard A. Pellegrino[2], Jonathan P. Leonard[2], John C. Wilson[1], Nancy J. Chanover[4], Peter Dow[1], Todd J. Henry[5], William Ketzeback[6], Devin McDonald[1], Russet McMillan[6], Jack Dembicky[6], Riley A. DeColibus[6], Candace Gray[6], and Amanda Townsend[6]
[1] Department of Astronomy, University of Virginia, 530 McCormick Road, Charlottesville, VA 22904, USA; jimmy@virginia.edu
[2] Department of Physics, Southern Connecticut State University, 501 Crescent Street, New Haven, CT 06515, USA
[3] NASA Goddard Space Flight Center, 8800 Greenbelt Road, Greenbelt, MD 20771, USA
[4] Astronomy Department, New Mexico State University, Las Cruces, NM 88003, USA
[5] RECONS Institute, Chambersburg, PA 17201, USA
[6] Apache Point Observatory, 2001 Apache Point Road, Sunspot, NM 88349, USA
Received 2023 November 6; revised 2024 January 9; accepted 2024 January 14; published 2024 February 19

Abstract

The Differential Speckle Survey Instrument (DSSI) was relocated to the Astrophysical Research Consortium 3.5 m telescope at Apache Point Observatory (APO) in early 2022. Here we present results from the first year of observations along with an updated instrument description for DSSI at APO, including a detailed description of a new internal slit mask assembly used to measure the instrument plate scale from first principles. Astrometric precision for DSSI at APO during this time was measured to be 2.06 ± 0.11 mas, with a photometric precision of 0.14 ± 0.04 mag. Results of 40 resolved binary systems are reported, including two that were previously unknown to be binaries: HIP 7535 and HIP 9603. We also present updated orbital fits for two systems: HIP 93903 and HIP 100714. Finally, we report updated or confirmed dispositions for five Kepler Objects of Interest (KOIs) that were previously explored in Colton et al., using speckle imaging to discern common proper motions pairs from line of sight companions: KOI-270, KOI-959, KOI-1613, KOI-1962, and KOI-3214AB.

Unified Astronomy Thesaurus concepts: Astronomical instrumentation (799); Speckle interferometry (1552); Astrometry (80); Binary stars (154); Exoplanet systems (484)

Supporting material: machine-readable table

1. Introduction

The Differential Speckle Survey Instrument (DSSI), was built at Southern Connecticut State University (SCSU) and was first commissioned at the WIYN 3.5 m telescope at Kitt Peak in 2008 (Horch et al. 2009). It was at the time the only speckle-imaging camera that could record speckle patterns in two colors simultaneously. The two-color approach proved useful in the reduction and analysis by providing more efficient use of telescope time, color information of any companion stars detected, and the ability to characterize binaries below the diffraction limit by using the two colors to tell the difference between residual atmospheric dispersion and true (blended) binarity (Horch et al. 2011b).

As discussed in Horch et al. (2011a), DSSI was used at WIYN for two primary purposes: (1) a large NSF-funded program of observations of nearby stars and (2) for follow-up observations of Kepler Objects of Interest (KOIs) to determine if these possible exoplanet hosts also had stellar companions. During these programs, the first major upgrade to DSSI occurred. The original detectors, which were a pair of Princeton Instruments CCD cameras, where upgraded to a pair of Andor iXon EMCCDs. This improved the overall detection limit of the system by approximately two magnitudes, from 12th magnitude to roughly 14th magnitude at WIYN.

Given the success DSSI enjoyed at WIYN, it was then used at the two 8.1 m Gemini telescopes from 2012 to 2018 as part of Gemini's Visitor Instrument Program. At the larger aperture, DSSI gave a competitive visible-light complement to large-aperture adaptive optics systems that were also vetting exoplanet candidate host stars with high-resolution observations. Example results include Horch et al. (2012), Crossfield et al. (2016), Mayo et al. (2018), and Kostov et al. (2019).

In 2016, a new speckle instrument, the NN-Explore Exoplanet Stellar Speckle Imager (NESSI), based on the DSSI design, was commissioned at WIYN (Scott et al. 2018). With this new speckle imaging for WIYN, DSSI was now available for use on yet another new telescope, the 4.3 m Lowell Discovery Telescope (LDT). Simultaneous to the Gemini work, the instrument was also used about four times a year at the LDT from 2014 to 2021, carrying out some of the same science as described above, but also initiating a volume-limited survey of K and M dwarf stars using speckle imaging and other techniques (see Horch et al. 2021 and references therein, as well as Clark et al. 2022).

The two Gemini telescopes commissioned their own speckle-imaging instruments based on the DSSI design in 2018. Zorro and 'Alopeke were installed on the Gemini South and North telescopes, respectively (Scott et al. 2021). Later, the

[7] Adjunct Astronomer, Lowell Observatory.
[8] Current address: Department of Astronomy, The Ohio State University, 4055 McPherson Laboratory, 140 West 18th Avenue, Columbus, OH 43210-1173, USA.

Table 1
Optical Elements in DSSI at APO

Element	Edmund Optics Stock Number	Size (mm)	Focal Length (mm)	λ (nm)	$\Delta\lambda$ (nm)	Peak Transmission (%)	Peak Reflection (%)	Thickness (mm)
Collimating Lens[a]	49–357	25.00	60	⋯	⋯	⋯	⋯	8.78[b]
Dichroic (Violet-Green)[c]	47–421			497		93	99	1.1
692 nm Filter[c]	48–148	25.00	⋯	692	40	99	⋯	3.5
880 nm Filter[d]	45–672	24.15	⋯	880	50	∼60[e]	⋯	∼7.5[e]
Reimaging Lenses[a]	45–179	50.00	200	⋯	⋯	⋯	⋯	9.11[b]

Notes. These are the optical elements used in DSSI at APO.
[a] New element for APO.
[b] Edge thickness.
[c] Original element from Horch et al. (2009).
[d] Non-original element first used in Horch et al. (2011b).
[e] Filter discontinued by Edmund; the estimated value is that of the current Edmund filter with the same bandpass and center wavelength.

LDT would commission the Quad-camera, Wave-front-sensing, Six-wavelength-channel Speckle Interferometer, whose design was inspired by DSSI, but has added two additional wavelength channels in the visible range, an infrared capability, and a wave-front sensor (Clark et al. 2020).

The inspiration DSSI provided at each of these facilities enabled the construction of the new speckle instruments, while making DSSI available for other opportunities. The latest is a new collaboration, started in 2021, between SCSU and the University of Virginia to use DSSI as a visiting instrument on the Astrophysical Research Consortium (ARC) 3.5 m telescope at Apache Point Observatory (APO) in New Mexico. DSSI was relocated from the LDT to APO in early 2022. In this contribution, we describe modifications to DSSI made for its use at APO, and present results from the first year of DSSI observations there.

2. Instrument Description

Here we present a description of the instrument in its current configuration at APO on the ARC 3.5 m telescope. Our discussion follows the optical path, from the telescope to the detectors, according to the original DSSI block diagram shown in Figure 1 of Horch et al. (2009). All optical elements are from Edmund Optics, and details are summarized in Table 1.

The ARC 3.5 m telescope is designed for quick instrument changes on one of its Nasmyth ports, known as the NA2 port, which is where DSSI mounts. Instruments have integrated mounted plates that facilitate this quick-change, allowing operators to change the instrument on the NA2 port in a matter of minutes. DSSI images the telescope focal plane, and therefore, to position DSSI's object focus to the location of the telescope focal plane, a short extension was installed between DSSI and the instrument mounting plate as seen in Figure 1. Similar extension mounts were built for DSSI at the LDT, WIYN, and the Gemini telescopes.

2.1. Optical Elements

The first optical element in DSSI is a 25 mm diameter MgF_2-coated achromatic lens with a 60 mm focal length used to collimate light from the telescope, referred to hereafter as the collimating lens. Various collimating lenses have been used in DSSI in the past, depending on the telescope, however, they were all the same diameter (25 mm) and used the same optomechanical mount. The focal length of the collimating lens used was chosen based on the f ratio of the telescope and the pixel size of the detectors, to ensure Nyquist sampling in the DSSI focal plane. Originally a 30 mm focal length lens was used at WIYN with the CCD cameras (Horch et al. 2009). When these CCDs, which had 13.5 μm pixels, were replaced by Andor iXon 897 EMCCDs having 16 μm pixels, the collimating lens was changed to a 35 mm focal length to maintain Nyquist sampling. The LDT used a 40 mm focal length lens, given the larger telescope aperture compared to WIYN, and Gemini North and South each used a 85 mm focal length lens.

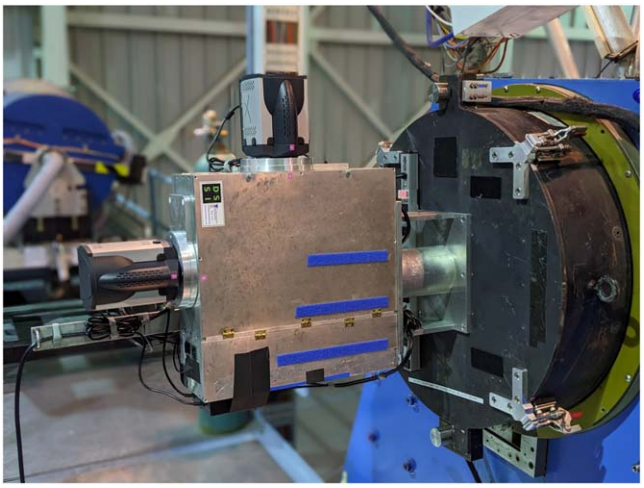

Figure 1. DSSI mounted to the Nasmyth port of the ARC 3.5 m telescope at APO. The instrument port has been rotated ∼90°.

Originally a space was left following the collimating lens for Risley prisms to be used for atmospheric high-dispersion compensation, however, these were never installed. In this location we have now mounted a custom fabricated slit mask assembly for plate scale calibration (see detailed discussion in Section 2.3).

The original tip-tilt mirrors (which was a galvanometric scanning mirror system) that came next were removed prior to bringing DSSI to APO. This is partly because the fast-readout EMCCDs no longer require multiple speckle patterns to be recorded across each frame, as was the case with the original, relatively slow-readout, CCDs. However, up until 2018, the Tip-Tilt mirrors had been installed and stowed in fixed positions. Eventually the mirrors began suffering from inadvertent movements during exposures. Because of this, the

assembly was replaced with a 3D-printed mount that holds the two flat mirrors in permanently fixed positions.

The next optical elements after the flat mirrors are the dichroic beam splitter and filters. A violet-green dichroic plate is mounted in an Edmund Optics 45° plate mount cube (Stock #56–264) with threaded ports used for installing pre-mounted filters. The transmission arm, which is referred to as Channel A, has a 692 nm narrow-band filter, while the reflected arm, referred to as Channel B, has a 880 nm narrow-band filter (see Table 1 for details). All observations from APO have been conducted using this default configuration; however, it is possible to change the dichroic and filters if desired.

The final optical elements are a pair of 50 mm diameter MgF_2-coated achromatic lens with a 200 mm focal length, one for each arm, to focus the collimated light from the instrument onto a pair of EMCCD detectors. These lenses have not changed from Horch et al. (2009).

2.2. Detectors

The original detectors on DSSI were Princeton Instruments PIXIS 2048B CCDs and were used from 2008 to 2010, when they were replaced by a pair of Andor Ixon 897 EMCCDs. Since moving DSSI to APO, we have installed a new pair of Andor Ixon 888 EMCCDs. There is a small improvement in performance compared to the older EMCCDs, including improvements to read noise and dark current; however one significant advantage to the new EMCCDs is the addition of a standard USB3.0 connection, compared to the previous generation EMCCDs, which only had Camera Link.

2.3. A New Internal Slit Mask

Accurate knowledge of the instrument plate scale is critical for precision astrometry. When DSSI was used on the WIYN telescope the plate scale was measured using a slit mask attached to the tertiary mirror baffle support. The method of measuring the plate scale via the fringes obtained by observing bright unresolved stars with a slit mask has been described by Horch et al. (2008). When DSSI was used at the LDT or Gemini, however, it was not possible to install a slit mask as had been done at WIYN. Instead, at these telescopes the instrument plate scale was measured using observations of multiple "scale" binaries having extremely well-known orbits. This method was first used by Horch et al. (2012) for DSSI observations from Gemini North, and the method has produced a precision of ∼1 mas for DSSI at Gemini, and ∼2 mas for DSSI at the LDT.

At APO, there was no existing slit mask, and, because of its quick instrument change operations model, it is not possible to have a slit mask for the tertiary mirror baffle support. We therefore initially relied on observations of "scale" binaries to measure the plate scale. However, during the first year of speckle observations at APO, we developed an internal slit mask assembly that is located in the collimated beam of the DSSI instrument, just after the collimating lens, in the space originally meant for the Risley prisms (which were never installed).

The slit mask is an air slit mask that we designed and had custom made by National Aperture. Their standard foil size was used, which has a diameter of 0.953 mm, and National Aperture mounted the foil in their 1 inch aperture mount. Figure 2 shows the slit mask design. The gray outer region

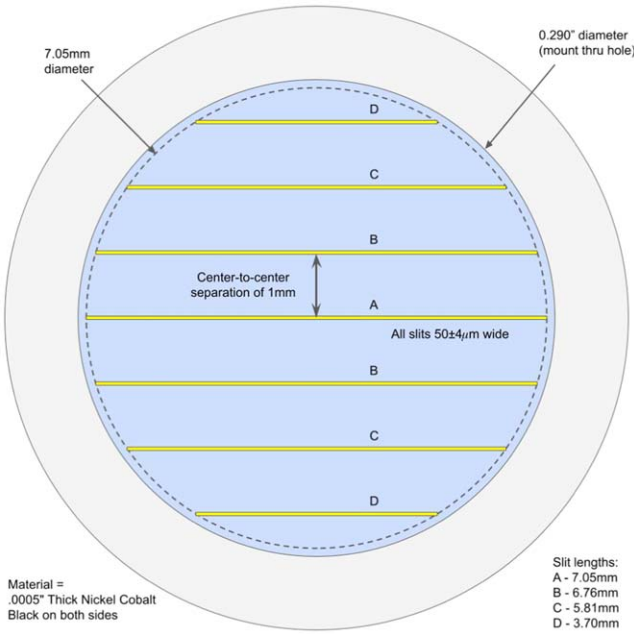

Figure 2. Slit mask design. Yellow bars show the air slits, while the blue region depicts the exposed region of the foil mask when mounted. All slits are 50 ± 4 μm wide, with a center-to-center separation of 1 mm.

represents the area of the foil covered by a retaining ring, while the blue region depicts the clear aperture of 7.3 mm. The slits are 50 ± 4 μm wide, with a center-to-center separation of 1 mm. Slits extend to a 7.05 mm diameter to allow for tolerances in the foil size when mounting to avoid distortion when the retaining ring is installed. The mask therefore contains seven slits of varying lengths, as depicted in Figure 2.

A Thorlabs dual-position slider with resonant piezoelectric motors holds the slit mask in one port, while the other port remains open, as seen in Figure 3. Normally the stage is positioned such that the collimated beam passes through the open port, and the slit mask is only inserted into the collimated beam during calibration frames. The stage is controlled remotely with the Thorlabs Elliptec Software, allowing insertion and removal of the slit mask at any time. This is more efficient and safer compared to installing a slit mask on the telescope tertiary baffle support.

Installation of the slit mask occurred at the start of the 2022 November observing run. We continued to observe "scale" binaries while we evaluated the performance of the slit mask. Slit mask observations are performed while observing a point source. To reduce overhead time, we choose to observe the same stars used as point source references for the "scale" binaries; thus, the observation sequence is (1) "scale" binary, (2) standard point source observation without the slit mask, (3) same point source with the slit mask installed. Because DSSI has a well-known scale distortion in channel B (Horch et al. 2017), we also periodically rotated the slit mask between nights and runs.

3. Data Reduction and Calibration

Observing time on the ARC 3.5 m at APO is scheduled quarterly and in half-night blocks. Observations were carried out with DSSI at APO over four separate observing runs during the first year: four half nights between 2022 May 10 and 15 UT; five half nights between 2022 September 27 and 30 UT;

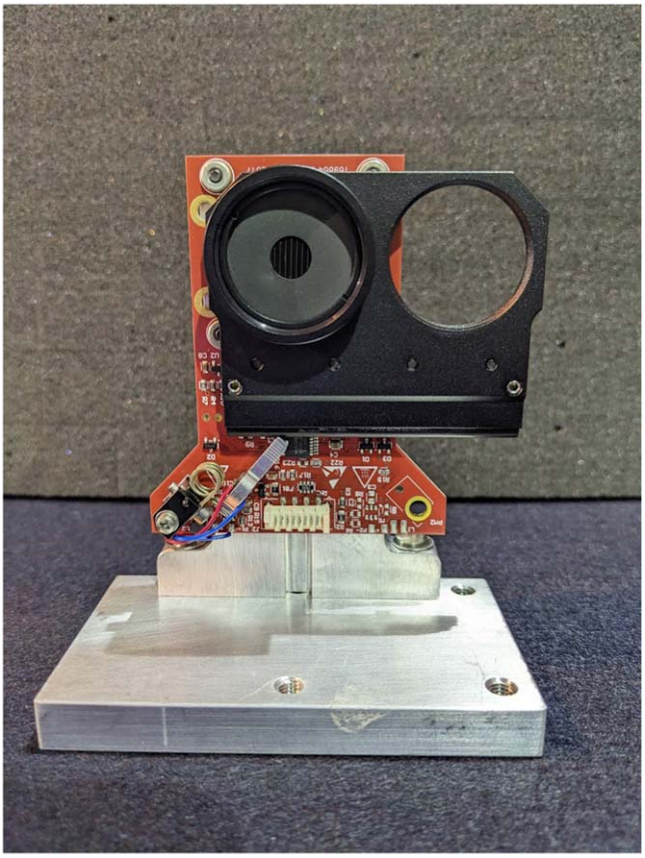

Figure 3. Slit mask assembly on lab bench prior to installation. The mask is installed in the left hand port of the dual-position slider, which is attached to an aluminum mount.

six half nights between 2022 November 12 and 16 UT; and five half nights between 2023 March 7 and 9 UT. Because the awarded time was not contiguous during these quarterly observing runs, DSSI was frequently dismounted from and remounted to the NA2 telescope port between half nights of observing.

3.1. Data Reduction

Despite DSSI's move to a new telescope, our data reduction methodology is the same as has been used for DSSI data taken at other telescopes. Most recently, this procedure was described briefly in Horch et al. (2021), but it dates back to the first use of EMCCDs with the DSSI optics and is fully described in Horch et al. (2011a) as a part of the WIYN observational program with the instrument. We briefly summarize the process here.

Both EMCCDs are operated using the Solis software from Andor. A sub-array of 256 × 256 pixels, centered on the target, is read out from each camera. Exposure times are generally 40 ms, however this is often increased to 100 ms for fainter targets. Electron-multiplying gains on the EMCCDs are chosen to give high speckle contrast; typically, bright objects are observed at low gain, where the device acts very similarly to a normal CCD, while faint objects are observed at high gain, where the device acts more like a photon counter. A single observation consists of 1000 frames per camera, meaning 1000 frames in the 692 nm filter and, simultaneously, 1000 frames in the 880 nm filter. A sequence of one to several thousand 40 ms frames is taken of an object. The number of frames as well as the EM gain factor for the observation is determined by brightness and seeing conditions, but generally objects fainter than magnitude 9–10 require the highest gain setting of our cameras; in poorer seeing or when observing through clouds, this transition point is at a brighter magnitude. Bright, single stars, used as point source calibration objects to obtain estimates of the speckle transfer function for the region of the sky where we are observing, are recorded with low EM gain. The data files for all observations are stored as FITS data cubes in blocks of 1000 frames per individual file.

From each image frame in the sequence, we form the spatial frequency power spectrum, and we sum all of these to obtain a final power spectrum from the observation. Computing the same for a suitable point source allows us to deconvolve the speckle signature from the data in the Fourier domain through simple division, and arrive at the pure power spectrum of the source. To minimize atmospheric dispersion effects, as a dispersion corrector is not used, we adopt a strategy of observing objects near the meridian whenever feasible. While dispersion will have a greater affect in the blue, we have found on 4 m class telescopes that, as long as the zenith distance is less than ∼60°, dispersion effects are minimal. This is the same strategy used at the comparable apertures of WIYN (e.g., Horch et al. 2011a) and the LDT (e.g., Horch et al. 2015), where results are well-established up to a zenith distance of ∼60°. Next, we form near-axis subplanes of the image bispectrum, so that phase information can be computed from the data set. We use the relaxation technique of Meng et al. (1990) to arrive at the object phase from the bispectrum, as first suggested in Lohmann et al. (1983). By taking the square-root of the power spectrum and combining it with the phase estimate, we can construct the Fourier transform of the object. We then low-pass filter the result with a 2D Gaussian filter, and inverse-transform to arrive at a reconstructed image. Typical examples of reconstructed images we obtain are shown in Figure 4.

In measuring position angles, separations, and magnitude differences of the components of binary and multiple star systems, we use the deconvolved power spectrum and fit fringes to that function in the Fourier domain, as first described in Horch et al. (1996). In cases where no companions are detected but the observation is of high quality (as evidenced by power out to near the diffraction limit in the Fourier domain), we use the reconstructed image to estimate the detection limit in magnitude difference from the primary star as a function of distance. This technique was described in Horch et al. (2011a), where pixels falling in concentric annuli centered on the target star are studied statistically, and local maxima and minima are used to arrive at 5σ detection limits.

3.2. Scale Calibration

When DSSI first arrived at APO, it did not have the slit mask described in Section 2.3, and scale calibration was instead handled by observing "scale" binaries with extremely high-quality visual orbits (often determined though observations made with long baseline optical interferometers); given their high quality, they could be considered definitive for our purposes. A list of objects used for this purpose is shown in Table 2. For the last two runs presented here, 2022 November and 2023 March, the slit mask was installed and used as a major part of the calibration process. However, in those two runs, we also observed calibration binaries in the same way, for

Table 2
Orbits and Residuals Used in the Scale Determinations

Run	Month and Year	WDS	Discoverer Designation	HIP	Besselian Year	$\Delta\theta_A$ (°)	$\Delta\rho_A$ (mas)	$\Delta\theta_B$ (°)	$\Delta\rho_B$ (mas)	Orbit References
1	2022 May	15232+3017	STF 1937AB	75312	2022.3557	−0.08	+0.4	−0.08	−0.2	Muterspaugh et al. (2010a)
					2022.3557	−0.08	+0.6	−0.08	+0.1	Muterspaugh et al. (2010a)
					2022.3586	−0.03	+0.1	−0.03	−0.9	Muterspaugh et al. (2010a)
					2022.3586	−0.03	−0.2	−0.03	−1.1	Muterspaugh et al. (2010a)
					2022.3586	+0.07	−0.2	−0.03	−0.7	Muterspaugh et al. (2010a)
					2022.3613	+0.13	+1.6	+0.13	+2.3	Muterspaugh et al. (2010a)
					2022.3613	+0.03	+2.8	+0.03	+0.8	Muterspaugh et al. (2010a)
					2022.3613	+0.13	−3.5	+0.13	−0.8	Muterspaugh et al. (2010a)
					2022.3694	+0.01	−1.4	−0.09	0.5	Muterspaugh et al. (2010a)
2	2022 Sep	15232+3017	STF 1937AB	75312	2017.3429	+0.2	−0.8	+0.1	−0.2	Muterspaugh et al. (2010a)
2	2022 Sep	21145+1000	STT 535AB	104858	2017.7968	0.0	−0.1	0.0	−0.2	Muterspaugh et al. (2008)
2	2022 Sep	22409+1433	HO 296AB	111974	2017.7969	0.0	+0.1	0.0	+0.2	Muterspaugh et al. (2010a)
3	2022 Nov	02278+0426	A 2329	11452	2017.7968	0.0	−0.1	0.0	−0.2	Mann et al. (2019)
3	2022 Nov	08122+1739	STF 1196AB	40167	2017.7968	0.0	−0.1	0.0	−0.2	Izmailov (2019)
3	2022 Nov	21145+1000	STT 535AB	104858	2017.7968	0.0	−0.1	0.0	−0.2	Muterspaugh et al. (2008)
4	2023 Mar	15232+3017	STF 1937AB	75312	2017.3429	+0.2	−0.8	+0.1	−0.2	Muterspaugh et al. (2010a)

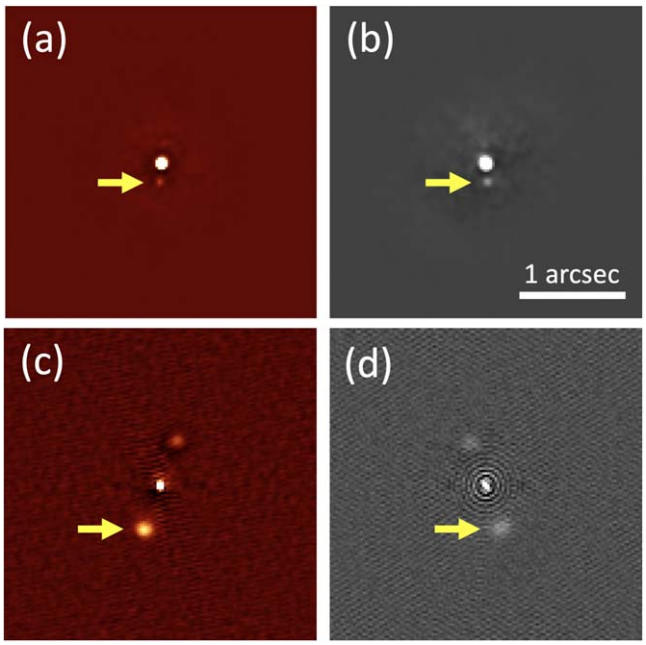

Figure 4. Reconstructed images for two objects appearing in Table 3. (a) The 692 nm image of HR 463, a fifth-magnitude star that we resolve for the first time in this image. (b) The 880 nm image of HR 463. (c) The 692 nm image of KOI-5822, a star with $G = 12.91$. (d) The 880 nm image of KOI-5822. A scale bar is shown in the lower portion of panel (b), but applies to all four images, and a yellow arrow shows the location of the secondary star. The 692 and 880 nm images appear as mirror images because the 880 nm channel reflects from the dichroic element in DSSI whereas the 692 nm light is transmitted. The images of KOI-5822 exhibit a feature common to our reconstructions of faint objects, where a low-level peak appears 180° away from the primary at the same separation due to low signal-to-noise phase information in the Fourier plane.

two reasons. First, we wanted to have cross calibration between the methods, and second, we had no way to easily rotate the slit mask during the night, so it was not possible to build up a complete picture of the scale as a function of position angle solely with the slit mask. Measuring the scale as a function of position angle is important because the dichroic element inside the DSSI optics package is known to have optical aberrations (e.g., astigmatism) in the reflective channel that alters the scale. More information on this effect for DSSI can be found in Horch et al. (2017).

To obtain scale and chip orientation angles from calibration binary data, we simply observe these stars in the normal way, and reduce the data as described in the previous subsection. We fit the fringes in the power spectrum of the binary, and then adjust the scale and orientation angle for the run to minimize the residuals of the group of calibration observations for a given run when comparing against ephemeris positions derived from the known orbital elements. We use the telescope's Nasmyth rotator to examine the dependence of the scale on position angle, deriving the parameters needed to characterize this effect for the reflective channel.

To obtain calibration data using the mask, we insert it into the collimated beam inside the DSSI optics box and we take a sequence of short-exposure frames of a bright, unresolved star in exactly the same way as described for science data. In this case, the power spectrum shows a sequence of lines at equally spaced intervals in the Fourier plane, and, using the predicted diameter of the collimated beam (based on the telescope diameter and f ratio, as well as the collimating lens's focal length), the known spacing of the slits, and the effective wavelength of the observation, we can derive a scale value from first principles. The effective wavelength is calculated by combining the filter transmission curve, the spectrum of a star of the same spectral type as the star observed, a typical atmospheric transmission curve, and the quantum efficiency curve of the detector. Examples of calibration data and fits are shown in Figure 5.

Analysis of both the slit mask binary data from 2022 November and 2023 March has revealed that there is a discrepancy in the scale between the channels. The transmissive channel (692 nm) agrees well with the calibration binary data while the reflective channel shows a slight systematic difference. Although this is still under study, the most likely explanation for this difference is that we do not have a measured curve nor a "typical" curve provided by the vendor for the transmission of the 880 nm filter. Therefore, to date, we have simply assumed a perfect "notch" filter of center wavelength 880 nm and width of 50 nm, which were values specified by the vendor. Given this deficiency, we assume here that slit mask data taken in the transmissive channel (i.e., at

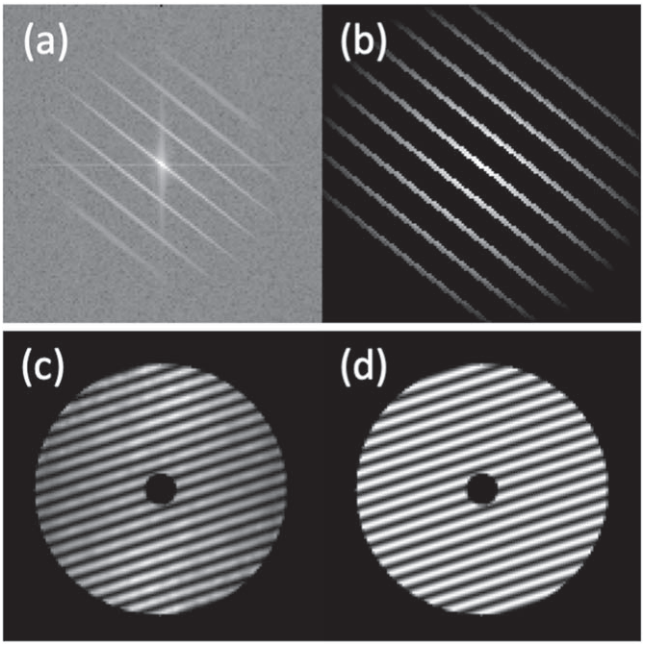

Figure 5. Typical examples of calibration data and fits for DSSI at the ARC telescope. (a) The slit mask power spectrum obtained for HR 3366 on 2023 March 7. (b) The derived best fit based on the slit mask model. (c) The power spectrum of the well-known binary η CrB (HIP 75312, STF 1937AB) obtained on 2023 March 9 is shown. (d) The fringe fit of η CrB.

692 nm) can be used as the benchmark for those data and then, to arrive at the pixel scale for the reflective (880 nm) channel, we compute the ratio of the scales derived from calibration binaries and apply that to the scale for the 692 nm data to derive a scale for the 880 nm channel. This should be robust against any systematic errors in using the ephemeris positions, since only the ratio is used and not the separation.

At this stage, we still compute orientation angles from the ephemeris positions of the calibration binaries, but we hope to implement a protocol to observe trailing stars across our detectors to independently measure the chip orientation for both channels. Likewise, in the coming months, we hope to obtain up-to-date transmission curves for both filters used here. If these changes can be implemented, we will have a system of astrometric calibration that is completely independent from previous observations and orbit calculations.

4. Results

Our final table of results obtained using the methods above is shown in Table 3. The columns show (1) the Washington Double Star (WDS) number (Mason et al. 2001),[9] which also gives the R.A. and decl. for the object in J2000.0 coordinates; (2) an identifier from a standard star catalog, usually the Bright Star Catalogue (i.e., Harvard Revised [HR]) number, the Henry Draper Catalogue (HD) number, or the Durchmusterung (DM) number of the object; (3) the discoverer designation; (4) the Hipparcos Catalogue number; (5) the Besselian date of the observation; (6) the position angle (θ) of the secondary star relative to the primary, with north through east defining the positive sense of θ; (7) the separation of the two stars (ρ), in arc seconds; (8) the magnitude difference (Δm) of the pair in the filter used; (9) the center wavelength of the filter (λ_c); and (10) the full width at half maximum of the filter transmission ($\Delta\lambda$). The position angle measures have not been precessed from the dates shown. Two pairs in the table have no previous detection of the companion in the *Fourth Catalogue of Interferometric Measures of Binary Stars* (Hartkopf et al. 2001b)[10] and we therefore propose discoverer designations of Virginia-Southern Connecticut (VSC) 1 and 2 here. VSC 1 has been recently confirmed as binary in a subsequent observation at APO with DSSI in 2023 September; VSC 2 has been confirmed in another observation obtained by two of us (T.J.H. and E.P.H.) that occurred before the observation presented here. Future papers will present the relative astrometry and photometry for these observations.

As discussed in the introduction, this paper describes initial observations with DSSI at APO; the majority of observations were taken either for the K star survey of Henry et al. (2022) or for eclipsing binary follow-up work being conducted at the University of Virginia. A detailed description of our results on these latter two projects will be presented in future papers when those surveys are complete; nonetheless, we can combine the results to date with the results presented here to give a clear picture of the capabilities of DSSI at APO. In Figure 6, we show two visualizations of the data. Figure 6(a) is a plot of the magnitude difference of systems resolved as binaries as a function of the log of the separation measured, while Figure 6(b) is a plot of the magnitude difference as a function of the system magnitude. Both results are similar to what has been reported for DSSI at WIYN and the Lowell Discovery Telescope. DSSI is able to detect companions fainter than $\Delta m = 3$ at or near the diffraction limit of the telescope at the wavelengths we use (black line in Figure 6(a)) and, in some cases, we can measure systems below the diffraction limit; however, the current data set happens to include only objects with Δm's up to 2 in that separation range. We have been able to resolve systems with magnitudes as faint as $V = 15$ and magnitude differences as large as 6. Thus, DSSI has maintained its large parameter space for companion detection in speckle imaging in the move to APO.

5. Analysis of the Data

5.1. Astrometric Precision

As in previous papers, we have used the dual-channel capability of DSSI to understand the fundamental precision represented in our observations. Each channel represents an independent measurement under identical observing conditions, but taken at a different wavelength. The difference between the separation (or position angle) obtained in one channel from values derived from the other channel should be zero on average with a standard deviation characterized by $\sqrt{2}\,\sigma$, where σ represents the internal precision of either channel. Using all of the data from Figure 6 (and not simply those in Table 3), we obtain the plots shown in Figure 7. Figure 7(a) shows separation differences and Figure 7(b) shows position angle differences, both as a function of average separation. As expected, the former shows no dependence on separation and has a near-zero mean value. Formally, the mean is 0.09 ± 0.22 mas, with a standard deviation of 2.92 ± 0.16 mas. The position angle plot also has mean value near zero, formally $0\overset{\circ}{.}035 \pm 0\overset{\circ}{.}103$, but shows a flaring out of the data points at small separation. This is also

[9] http://astro.gsu.edu/wds/

[10] http://astro.gsu.edu/wds/int4.html

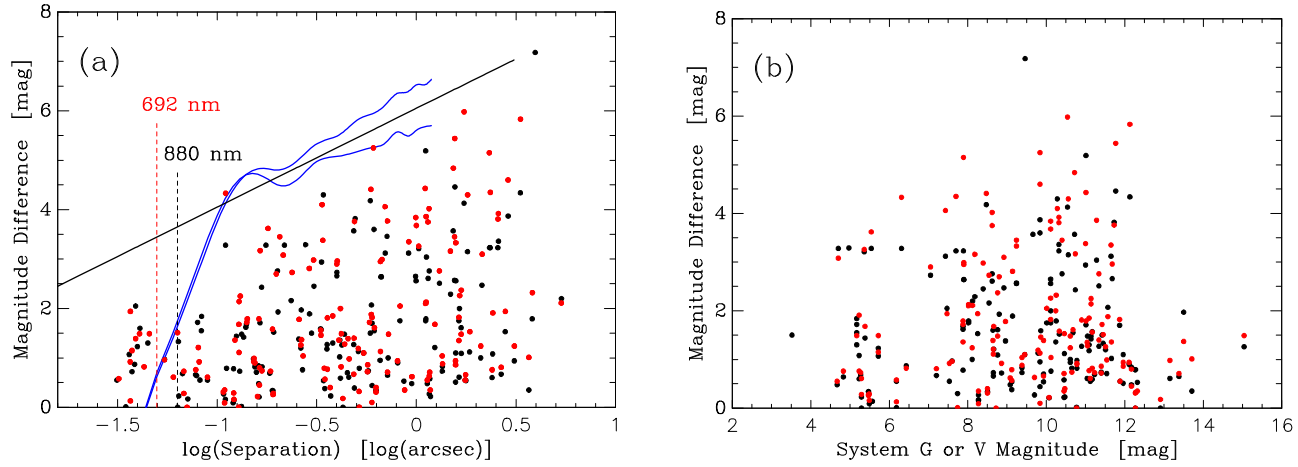

Figure 6. (a) Magnitude difference as a function of separation for all observations from the first year of operation. (b) Magnitude difference as a function of system V magnitude. In both panels, the color of the plot symbol indicates the filter wavelength used for the observation: red is 692 nm and black is 880 nm. Dashed vertical lines show the diffraction limit of the ARC 3.5 m telescope for the corresponding wavelength. In (a), the blue curves indicate typical detection limit curves for APO observations (see Horch et al. 2015 for details on how these are created) and the black line is the estimated detection limit for DSSI on the ARC 3.5 m telescope, drawn such that it roughly matches the blue curves above a separation of $0\farcs1$.

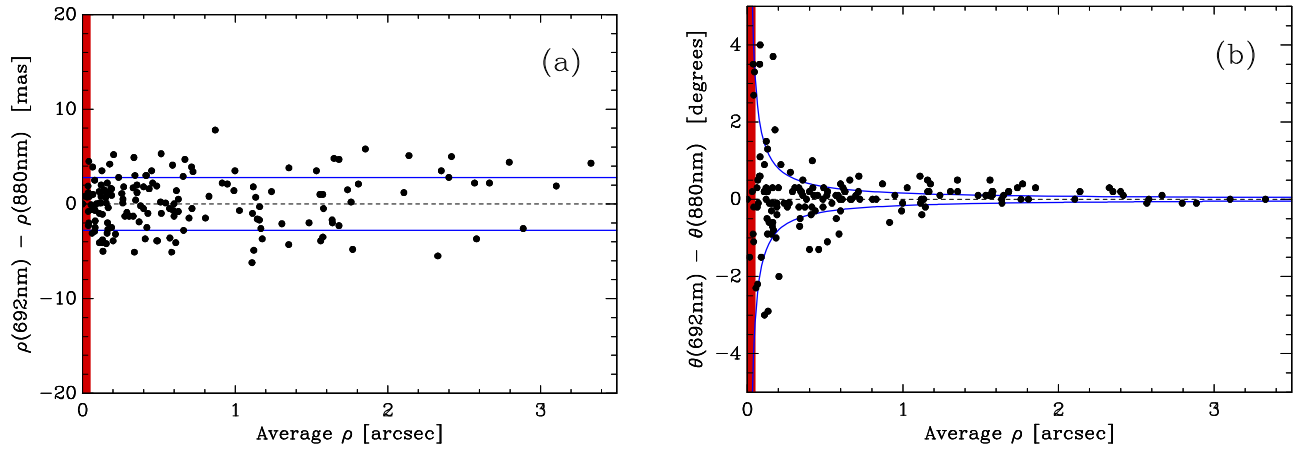

Figure 7. Differences in the astrometric results obtained between paired DSSI observations at the same epoch. (a) Differences in separation as a function of average separation. (b) Differences in position angle as a function of average separation. In both plots, a dashed line at a difference of zero is drawn to guide the eye, and the blue curves indicate the $\pm1\sigma$ in estimated internal repeatability of individual measures as a function of separation as discussed in the text. For differences in separation, that repeatability metric is simply the standard deviation of the measures and, for position angle, it is proportional to $\arctan(\delta\rho/\rho)$. In both (a) and (b), the red bar at the left marks the region below the formal diffraction limit.

Table 3
APO Binary Star Speckle Measurements

WDS (α, δ J2000.0)	HR, ADS DM, etc.	Discoverer Designation	HIP	Date (2000+)	θ (°)	ρ ($''$)	Δm (mag)	λ_c (nm)	$\Delta\lambda$ (nm)
01057+2128	HR 310	YR 6	5131	22.8645	136.8	0.0680	0.73	692	40
				22.8645	136.3	0.0670	0.68	880	50
01371+1209	HR 463	VSC 1	7535	22.8647	187.1	0.1800	3.62	692	40
				22.8647	185.3	0.1758	3.28	880	50
02035+0426	G 159-30	VSC 2	9603	22.8649	329.1	0.2062	3.45	692	40
				19.0505	331.1	0.2010	2.76	880	50

Notes.
[a] Quadrant determination of the secondary is ambiguous; the position angle could be the value listed $\pm180°$.
[b] Quadrant determination inconsistent with other published measures in the Fourth Interferometric Catalog.
[c] Photometry appears as an upper limit because the observation may be affected by speckle decorrelation as discussed in the Section 5.2.
[d] This observation was taken with the NESSI speckle camera at WIYN.

(This table is available in its entirety in machine-readable form.)

Table 4
Objects Used in the Astrometric Accuracy Study

WDS (α, δ J2000.0)	HR or ADS	Discoverer Designation	HIP	Orbit Grade	Orbit References
02278+0426	ADS 1865	A 2329	11452	1	Mann et al. (2019)
02396 − 1152	HR 781	FIN 312	12390	1	Docobo & Andrade (2013)
08122+1739	ADS 6650	STF 1196AB	40167	1	Izmailov (2019)[a]
13396+1045	ADS 8987	BU 612AB	66640	1	Mason et al. (1999)
17080+3556	ADS 10360	HU 1176AB	83838	1	Muterspaugh et al. (2010a)
18439 − 0649	HR 7034	YSC 133	91880	2	Horch et al. (2021)
20375+1436	ADS 14073	BU 151AB	101769	1	Muterspaugh et al. (2010b)
23052 − 0742	ADS 16497	A 417AB	113996	1	Hartkopf et al. (1996)

Note.
[a] This object was not used in the astrometric accuracy study because the derived uncertainty in position angle for our observation was much larger than for the other stars in this list.

expected, because a fixed linear separation uncertainty will subtend a larger angle if the separation is smaller, so that

$$\delta\theta = \arctan\left(\frac{\delta\rho}{\rho}\right). \quad (1)$$

In Figure 7(b), we show the expected flaring given a linear measurement precision of 2.9 mas and this matches the data set very well. Since the differences plotted here will have scatter that is $\sqrt{2}$ larger than the intrinsic scatter for a single channel, we conclude that the measurement precision for DSSI at APO is $\delta\rho = 2.92/\sqrt{2}$ or 2.06 ± 0.11 mas.

5.2. Astrometric Accuracy

To establish the accuracy of our measurements, we compare our results in Table 3 to ephemeris predictions for cases where a Grade 1 or Grade 2 orbit exists in the *Sixth Catalog of Visual Orbits of Binary Stars* (Hartkopf et al. 2001a).[11] The scale calibration stars listed in Table 2 are also of Grade 1, but the objects used there are of the highest quality as judged by the ephemeris uncertainties in ρ and θ; on the other hand, most of the objects used in this section are generally of slightly lower quality, but still useful as a check once the scale and detector orientation have been established. There are two objects that appear in both tables: A 2329 and STF 1196AB. In these cases, measurements appear in Table 3 because those observations were not used in the scale determination for the run in which the observation occurred. For example, A 2329 was used as a scale calibration object in 2022 November, but not in 2022 September even though it was observed. Since A 2329 was not needed for the scale determination in September, we find it permissible to include its measurements in Table 3 and to use them for this astrometric accuracy study.

As in previous papers, our strategy is then to average the astrometric results taken in both filters for each observation and compare this mean with the ephemeris prediction. Averaging should, in theory, provide for an additional decrease in the uncertainty by a factor of $\sqrt{2}$, meaning that the predicted uncertainty in separation measures due to our intrinsic precision in this case will be 1.46 ± 0.08 mas. There are eight objects in Table 3 that have a Grade 1 or 2 orbit, as listed in Table 4. However, in the case of STF 1196AB, using the reported uncertainties in the orbital elements leads to a large uncertainty in the position angle for the epoch of our observation, and so we have removed this object from the accuracy study. For BU 151AB, we do not have a 692 nm observation reported in Table 3. Our 692 nm observation had unusual systematics in the power spectrum that prevented a robust fringe fit. Thus, we have no way to average the results from both channels, as for other objects. Thus, we include the 880 nm observation in the study as is, without averaging.

In Figure 8, we plot the residuals in separation and position angle for all observations of these seven systems appearing in Table 3. Formally, the average residual in separation is 0.26 ± 1.22 mas, and the standard deviation is 4.22 ± 0.86 mas. In position angle, the results are $-1\overset{\circ}{.}24 \pm 0\overset{\circ}{.}82$ for the mean residual and $2\overset{\circ}{.}84 \pm 0\overset{\circ}{.}58$ for the standard deviation. The position angle values, in particular, are affected by the observations of YSC 133, which are below the diffraction limit. If we confine our attention to the orbits with the smallest uncertainties—for example, less than 2 mas in separation and less than 1° in position angle (red points in Figure 8)—then these numbers become $\overline{\Delta\rho} = 1.29 \pm 1.21$ mas, $\sigma_\rho = 3.83 \pm 0.86$ mas, $\overline{\Delta\theta} = 0\overset{\circ}{.}23 \pm 0\overset{\circ}{.}52$, and $\sigma_\theta = 1\overset{\circ}{.}48 \pm 0\overset{\circ}{.}37$.

While these numbers offer no evidence for large systematics in either position angle or separation, the average residual values here are larger than for the internal precision discussed in the previous subsection. At least some of this difference is probably attributable to small systematic differences in recent observations of these stars versus the orbital ephemerides. A typical example is BU 612AB. This system has an orbit due to Mason et al. (1999), where observations after 2010 show small trends in the observed minus ephemeris residuals, approximately +0.6 mas in separation and $-0\overset{\circ}{.}8$ in position angle). Figure 8 includes error bars on each point that represent the uncertainty derived from the orbital elements, so the residual from the "true" orbit can lie anywhere within that interval. If we count up the number of points whose error bars overlap with the expected uncertainties from our internal measurement precision study, slightly less than half of the points meet this criterion, whereas, if both orbital uncertainties and our measurement uncertainties are correct, about two-thirds should be consistent with the area marked for the internal measurement precision. Although the number of points here is small, the data at hand suggest that either our calibration and measurement process leads to slightly larger absolute errors than the repeatability study in the previous subsection suggests, or the declared uncertainties on the orbital elements of the objects we have studied are slightly underestimated, or both. The former would not be unexpected for a new astrometric

[11] https://crf.usno.navy.mil/wds-orb6

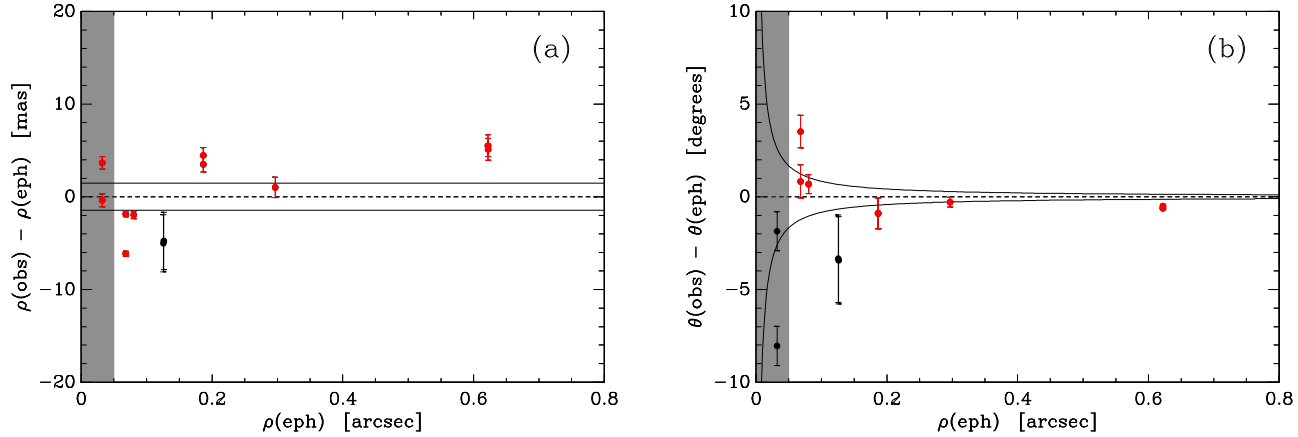

Figure 8. Residuals for objects in Table 3 having Grade 1 or Grade 2 orbits in the Sixth Orbit Catalog. (a) Observed minus ephemeris residuals in separation as a function of average separation. Points drawn in red indicate systems with ephemeris uncertainties of less than 2 mas. (b) Observed minus ephemeris residuals in position angle as a function of average separation. Points drawn in red indicate systems with ephemeris uncertainties of less than 1°. In both plots, our results in the two filters are averaged for a final result, a dashed line at a difference of zero is drawn to guide the eye, and the curves indicate the $\pm 1\sigma$ in estimated uncertainty in our measures as discussed in the text. In both (a) and (b), the gray bar at the left marks the region below the formal diffraction limit.

program; we will continue to study this situation in future observing runs.

5.3. Photometric Precision and Accuracy

In analogy to the analysis of astrometric precision in the previous subsections, we can establish the internal repeatability (precision) of the photometric measures in Table 3 through repeat observations, and examine accuracy through comparison with previous measurements obtained in other ways. Beginning with the internal repeatability, we have very few examples of repeat observations in the same filter, so no statistically robust conclusion can be drawn at this point; only A 417AB, BU 612AB, HU 1176AB, CHR 63, YSC 133, and STF 2383AB have more than one measurement in each filter. The last of these objects has the differential photometry shown as an upper limit in Table 3 for reasons we will discuss below, and YSC 133 is below the diffraction limit, and is not expected to have the same precision as measurements above the diffraction limit. For the other four objects, we can compute the average difference between the two measures in a given filter and its standard deviation as a first estimate of our photometric measurement precision. For the 692 nm filter, we obtain a mean difference of 0.03 ± 0.14 mag, and for the 880 nm filter, the mean difference is 0.09 ± 0.07 mag. For the standard deviations, we obtain 0.28 ± 0.10 and 0.13 ± 0.05, respectively. Averaging between the channels in the case of the standard deviation, we have 0.21 ± 0.06. Making the same argument that these are differences obtained from independent measurements drawn from the same distribution, the standard deviations here should be a factor of $\sqrt{2}$ larger than the intrinsic spread of the distribution of single measurements, so we obtain 0.14 ± 0.04 mag as the estimate of the typical internal precision for our photometric measurements. This is comparable to what was reported in earlier papers in this series at both the WIYN and the Lowell Discovery Telescopes.

To investigate the accuracy of our photometry is somewhat problematical, because it requires comparing to measurements made in other filter systems. Here we provide a brief comparison with Hipparcos and Gaia photometry, where it exists. Hipparcos data are in the H_p passband, a broadband filter centered at 511 nm, whereas Gaia data are reported in the G filter (or, in some cases, the R_p filter, but that is a very limited subset for our objects). Figure 9(a) shows this comparison for all objects in Table 3 that have either an ΔH_p or ΔG value. The horizontal axis of the plot is the seeing times separation of the binary, which in previous papers we have argued is proportional to the isoplanatic angle for the observation (e.g., Horch et al. 2004). The plot here shows a similar trend to that shown in previous papers in this series, where measures below seeing times separation of 0.6 arcsec^2 cluster near zero difference, but as the x-value grows, the speckle magnitude difference is generally larger than the space-based value, leading to an upward drift of data points. The reason is well known: if the secondary lies outside the isoplanatic angle, then there will be a decorrelation between speckles from the primary star and those of the companion, leading to weaker peaks in the autocorrelation function, and ultimately, a higher value for the derived magnitude difference. This is the reason that, in Table 3, we state magnitude differences as upper limits in some cases. For these observations, the seeing times separation is larger than 0.6 arcsec^2, and thus the value may be overestimated.

In Figure 9(b), we plot the space-based magnitude difference as a function of the speckle magnitude difference at 692 nm; these show a roughly linear trend with slope near 1. It is difficult to draw strong conclusions from this plot due to the color differences between the filters; formally, the standard deviations of the differences between our measures and Hipparcos is 0.32 ± 0.05 mag while, for the Gaia sample, it is 0.35 ± 0.05 mag. As can be seen from the plot, the uncertainties for the Hipparcos measures are generally much larger, but they populate the lower end of the seeing times separation and in fact represent many examples of subarcsecond separation systems. On the other hand, the Gaia measures have smaller uncertainties but mainly populate the region of seeing times separation of 0.4–0.6, and there are only a few examples of subarcsecond systems. The Gaia subset also likely contains more line of sight (LOS) companions, meaning more cases where the two stars in a given system have different colors. As magnitude difference is wavelength dependent, and we are comparing magnitude differences in the DSSI 692 nm narrow-band filter to those of the very broad Gaia G filter, the higher amount of scatter may be caused by the range in colors of the two stars in these systems. In the case of the Hipparcos

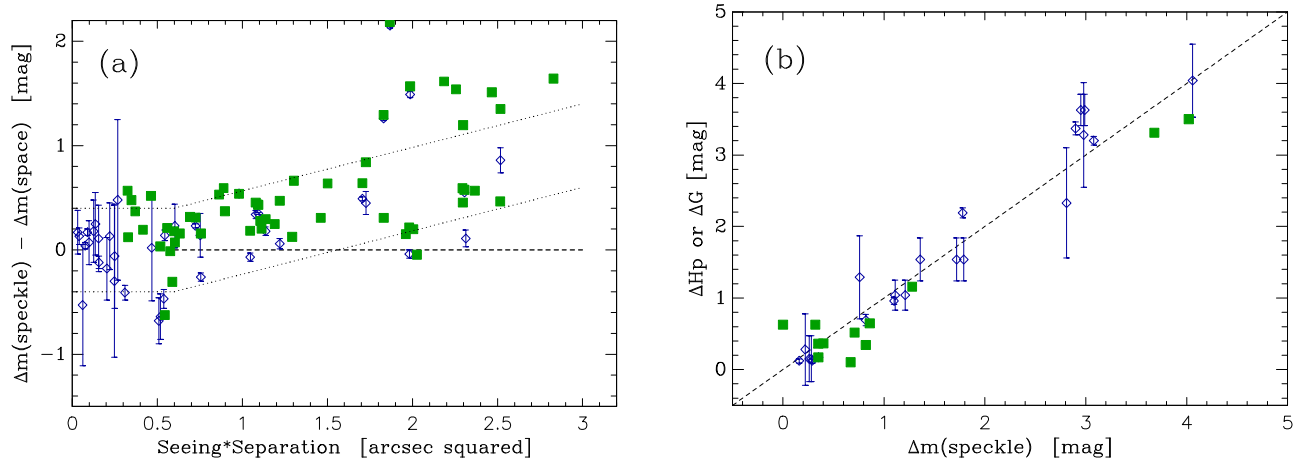

Figure 9. A comparison of photometric results obtained here with those of both Hipparcos and Gaia. (a) Magnitude difference in the 692 nm filter as a function of seeing times separation. The dotted blue lines indicate the approximate range of points in the same plot in our previous paper in this series (Horch et al. 2021). (b) For those systems with seeing times separation less than 0.6 arcsec^2, the space-based magnitude difference is shown as a function of the speckle magnitude difference at 692 nm. Here, the dotted line indicates the line $y = x$. In both plots, the open blue diamonds are derived from Hipparcos data and the filled green squares are derived from Gaia DR3 results. The error bars for Hipparcos points are those stated in the Hipparcos Catalogue, and the errors listed in the DR3 catalog for the Gaia points are typically smaller than the plot symbol.

Table 5
Visual Orbital Elements for Two Systems

Name	Spectral Type[a]	HIP	P (yr)	a ($''$)	i (°)	Ω (°)	T_0 (BY)	e	ω (°)
STA 3	B6IV	93903	27.89 ± 0.17	0.0728 ± 0.0069	127 ± 16	342.3 ± 7.8	2024.76 ± 0.46	0.781 ± 0.042	98.2 ± 5.6
A 730	A2IV	100714	90.42 ± 0.51	0.1378 ± 0.0055	180 ± 11	125 ± 36	2021.86 ± 0.15	0.681 ± 0.014	333 ± 53

Note.
[a] From SIMBAD (Wenger et al. 2000).

objects, if we assume that the speckle uncertainty would add in quadrature with the Hipparcos uncertainty to arrive at the standard deviation we obtain, then we can subtract the average Hipparcos $\delta(\Delta m)$ from that value to estimate the contribution to the standard deviation from the uncertainty in our measures. The result is 0.16 mag, which is consistent with the figure for our internal precision.

6. New Orbit Calculations

Using our new observations, we find we are able to update orbital information for two systems in the literature, both of which have evolved primary stars. The orbital elements that we derive are shown in Table 5.

6.1. HIP 93903 = HR 7262 = STA 3

This is a system with composite spectral type of B6IV with magnitude difference of about 1.5. The orbit of Hartkopf & Mason (2014) gives a period of 216.93 yr, but our data from 2022 November show a large discrepancy with this orbit, along with some other points in the literature that have large residuals. Given the Gaia DR3 parallax of 3.3932 ± 0.2262 mas, the implied mass sum is 2.77 $M_\odot$, which is quite low given the spectral type. Using the parallax and the apparent magnitude, the absolute visual magnitude is −2.094 while the magnitude difference is ∼1.5; we might therefore speculate that the system consists of a B5IV primary and a B8V secondary. This implies a mass sum in the range of 10 $M_\odot$.

These facts suggested that attempting a new orbit calculation could be fruitful. In addition to the APO data, we also had observed this star in the time frame of 2016–2017 from the WIYN Telescope using the NESSI speckle camera (Scott et al. 2018). In the data from the literature, there is a gap of 13 yr in the data from 1992 to 2005, and prior to fitting, we tried a quadrant flip starting at that point, so that most of the observations would have a position angle in the first quadrant. This was an attempt to see if a shorter period could make sense with the observations. We also find several points from 1-m class telescopes, where the separation would be very challenging to measure and the points appear to have considerable scatter. Removing those, but including the APO data point from 2022 November as well as the WIYN points mentioned, and refitting the orbit using the code of MacKnight & Horch (2004), we find the orbital elements shown in Table 5, where the period is 27 yr. This much lower period increases the implied mass sum to $12.7 \pm 4.4 M_\odot$. Both the old and new orbits are shown in Figure 10. We regard the new orbit as tentative; it is likely that, even if the quadrants assigned to the observations here are correct, future observations will lead to a subsequent orbit revision, and we encourage other observers to continue to study this system.

6.2. HIP 100714 = A 730

A 730 is an A2IV star with a magnitude difference of approximately 0.75 mag in the V band; it has a parallax of 3.6439 ± 0.1359 mas from the Gaia DR3 catalog. The visual

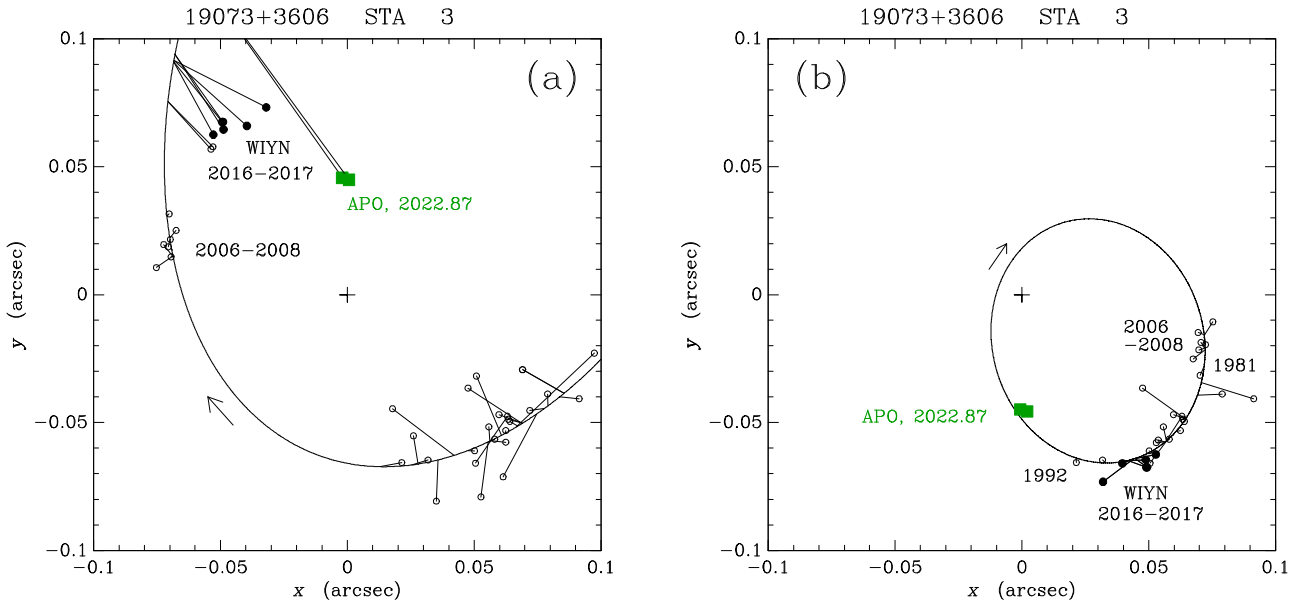

Figure 10. Orbit of STA 3 = HIP 93903. (a) The orbit calculated by Hartkopf & Mason (2014), together with the available observational data. (b) The orbit revision proposed here, which has a much shorter period and implies a much higher mass sum, as described in the text. Here, a quadrant flip is proposed for observations after 1992. In both plots, the cross marks the origin of the relative orbit, the open circles represent data points in the literature, the filled circles indicate observations taken at WIYN and appearing in Table 3, the green squares are the results from APO, and an arrow indicates the direction of orbital rotation (clockwise). Line segments are drawn from the ephemeris position on the orbit to the data point in each case. North is down, east is to the right.

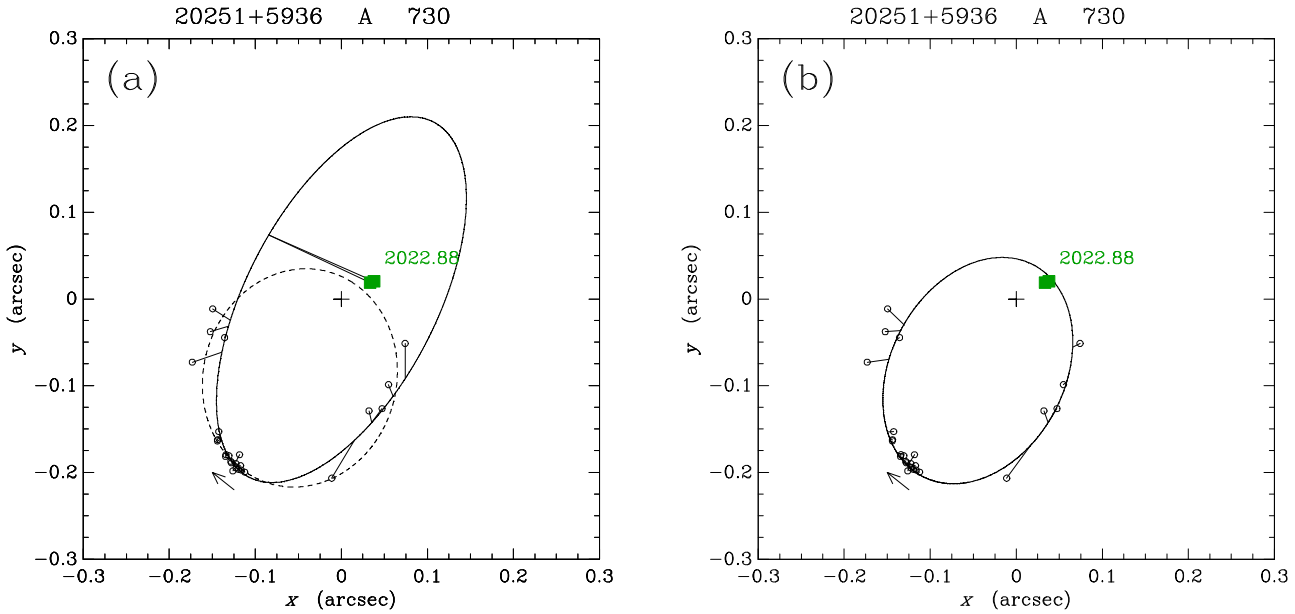

Figure 11. Orbit of A 730 = HIP 100714. (a) The two orbits calculated by Prieur et al. (2010). In that work, the authors suggested that the longer period orbit, shown here with the solid ellipse, was more likely, but they also calculated a shorter period orbit shown here as the dashed ellipse. (b) The orbit revision proposed here, which is much closer to the short period orbit of Prieur et al. (2010). In both plots, the cross marks the origin of the relative orbit, the open circles represent data points in the literature, the green squares are points appearing in Table 3, and an arrow indicates the direction of orbital rotation (clockwise). Line segments are drawn from the ephemeris position on the orbit to the data point in each case. North is down, east is to the right.

companion has been known since the 1930s and an analysis of the relative motion of the two stars was given in Prieur et al. (2010). Those authors propose two possible orbital periods, one of 88 yr and the other of 175 yr. They indicated that the larger period was probably more likely as the mass sum derived was close to the expectation for an A2IV star plus a companion at modest magnitude difference, but they also state that radial velocity variations permit the possibility of a third body in the system. In the intervening time, Fekel and Willmarth studied the system with spectroscopy and have determined that *both* visual components are in fact spectroscopic binaries with periods of a few days (F. C. Fekel 2024, private communication).

Combining the data appearing in Table 3 with data from the literature for this system, we refit the visual orbit and find an orbital period of 90 yr. Figure 11 shows the new orbit, along with the orbits from Prieur et al. (2010) where the new data rule out the longer period orbit based on the placement of the observations. Our implied mass sum is $6.6 \pm 1.1 M_{\odot}$. The absolute magnitude of the system is −0.75, whereas one would expect something more like 0.5 based on the composite spectral

Table 6
Updated Properties of Five KOI Double Star Components

KOI No.	Kepl. No. or Disp.[a]	No. of Planets	Distance (pc)	M_1[b] ($M_\odot$)	M_2[b,c] ($M_\odot$)	R_1	R_2	Prev. Disp.	Updated Disp.
270	449	2	260.11 ± 13.15[d]	0.84	0.77	0.0535 ± 0.0026	0.718 ± 0.067	CPM	CPM
959	PC		35.662 ± 0.053	0.24	0.22	0.0069 ± 0.0011	0.168 ± 0.038	Uncertain	CPM
1613	907	1	$492.5^{+161.2}_{-97.4}$	1.19	0.87	0.1822 ± 0.0300	3.756 ± 1.525	CPM	Orb. Mot.?
1962	PC		1101^{+629}_{-294}[d]	1.05	1.02	0.0840 ± 0.0132	2.086 ± 1.185	Uncertain	CPM
3214AB	PC		$471.3^{+95.3}_{-67.9}$	1.05	0.78	0.0684 ± 0.0528	0.661 ± 0.537	CPM?	CPM

Notes.
[a] If no Kepler number is given, the disposition as a planetary candidate (PC) is given, based on information available on the Kepler CFOP website.
[b] The uncertainty in all values in this column is assumed to be $0.1 M_\odot$.
[c] Calculated under the assumption that the companion is bound.
[d] No Gaia DR3 parallax is available. The distance for this system is taken from the CFOP website in the case of KOI-270 and from Gaia DR2 in the case of KOI-1962.

type and the magnitude difference, if there were only two stars in the system. Likewise the mass for just the visual primary and secondary would be on the order of 5 $M_\odot$, leaving room for the (unresolved) spectroscopic components.

7. Update on Five Kepler Stars

Using speckle data collected mainly at the WIYN telescope, Colton et al. (2021) attempted to categorize 37 KOIs that are small-separation double stars as either common proper motion (CPM) pairs or LOS companions. As discussed in their paper, they used the available astrometry to compare the proper motion of the system (or the primary if available) to the relative proper motion of the pair. By developing two criteria, which they called R_1 and R_2, Colton et al. estimated how likely the system was to be either LOS or CPM. The quantity R_1 is simply the ratio of the relative proper motion to the system proper motion. Systems with smaller values of R_1 are more likely to be CPM pairs; Colton et al. show that only 5% of hypothetical LOS companions would have an R_1 value less than 0.32. In contrast, the quantity R_2 compares the relative proper motion to the expected average change of position per year if the pair is gravitationally bound. Using a simulation based on known orbital statistics of solar-type stars, Colton et al. found that there was a 95% probability of a system being gravitationally bound if R_2 was less than 1.87. Of the 37 systems studied, 21 were determined to be either CPM pairs or probable-CPM pairs, and four were found to be LOS companions. Thus the fraction of systems that are likely bound from that subsample was above 80%. (The remaining 12 systems were characterized as "uncertain.")

Using our observations from APO, we are able to recalculate R_1 and R_2 values for five pairs studied in Colton et al. (2021), and to provide updated dispositions. Table 6 shows these new results. In three cases where the previous determination could not be made, we find that the system is a CPM pair, strengthening the result that most KOI found to be binary in high-resolution ground-based observations are in fact bound, as first suggested by Horch et al. (2014) using a statistical argument. The two remaining updates concern objects that Colton et al. (2021) proposed as candidates for orbital motion in the coming years. We find that there is now evidence of nonlinear relative motion in one case, but that in the other, the pair continues to exhibit linear motion at this time.

7.1. Common Proper Motion Binaries

We briefly discuss three objects that we can now confirm as CPM pairs, based on the new observations. Plots showing the relative motion in both R.A. and decl. for each system are shown in Figure 12.

1. KOI-959 (TIC 158490401). This M1 star has a very high proper motion (roughly 0.″5 per year), indicating that it is close by, yet it had no parallax result in the DR2 Gaia release. However, a large parallax value is reported in Gaia DR3. Using that, it is possible to now complete the calculation for R_2 described above, and thus to characterize this object. The relative motion is small compared to the system motion, as it was in Colton et al. (2021) and is only modestly updated here, making the determination of the system as a CPM pair quite robust. Due to its proximity, this pair joins the two objects in the next subsection as members on the watch list for orbital motion.
2. KOI-1962 (TIC 120107336). No spectral type is given in SIMBAD, but the $B - V$ color suggests mid-G range as the likely composite spectrum. The system sits at a distance of approximately a kiloparsec (with large uncertainty), and together with the apparent V magnitude of 11 and the small magnitude difference of the components, it would appear possible that both the primary and secondary stars are evolved.

   With the addition of the APO observations presented here, the relative proper motion values for this system have decreased, resulting in lower values for both R_1 and R_2 compared to those reported in Colton et al. (2021). These values now meet our definition of a CPM pair: $R_1 + \delta R_1 < 0.32$ and $R_2 - \delta R_2 < 1.87$.
3. KOI-3214AB (TIC 268160366). This system is a triple, with the B component at approximately 0.″5 from the primary and the C component at 1.″3. In Colton et al. (2021), the inner component's status is listed as a probable-CPM pair; this is now confirmed as a CPM with our observations. The wider component remains more difficult to characterize; a large uncertainty in the relative proper motion prevents the CPM determination at present.

7.2. Two Binaries that are Candidates for Orbital Motion

In Colton et al. (2021), two double stars were highlighted as the most likely to exhibit measurable orbital motion in the

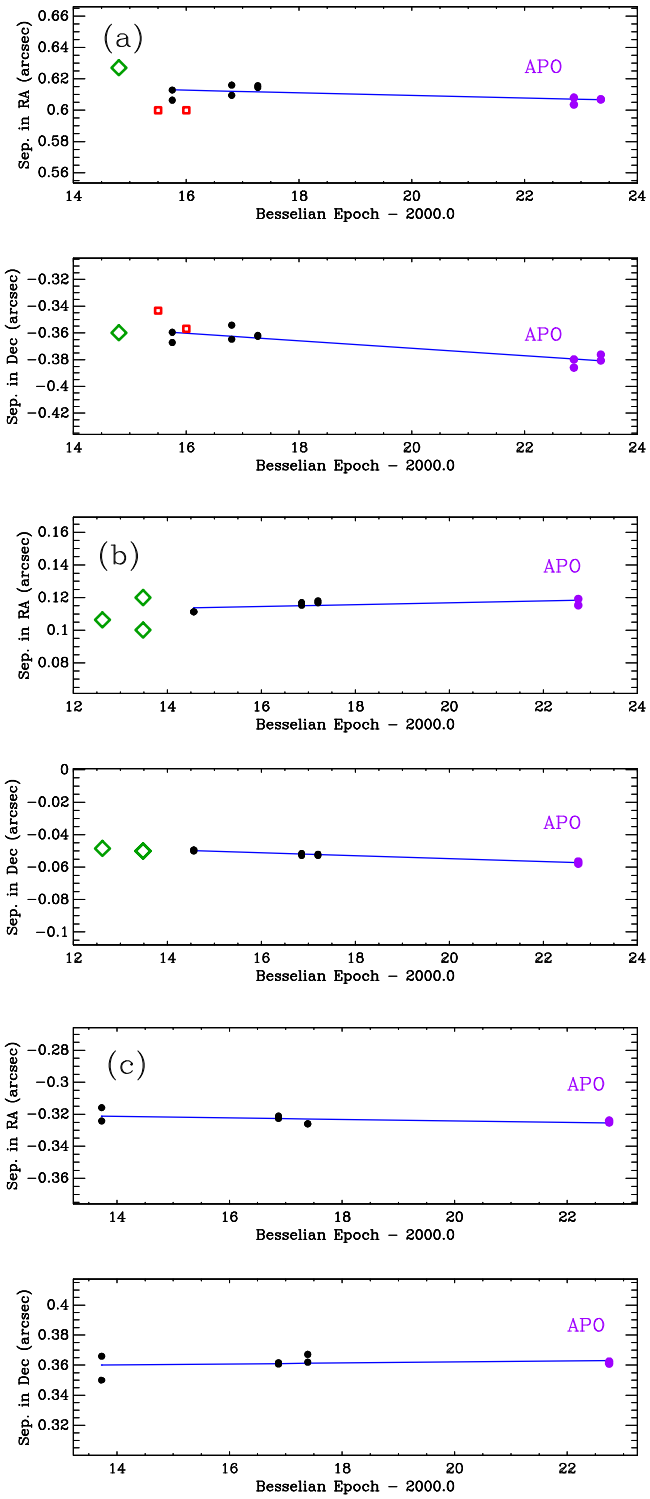

Figure 12. Motion of the stellar secondary relative to the primary for the three CPM systems discussed in Section 7.1: (a) KOI-959; (b) KOI-1962; and (c) KOI-3214AB. In all plots, the filled circles represent observations taken earlier in our program and reported in Colton et al. (2021), the purple filled circles on the right marked "APO" indicate the new data appearing in Table 3, green diamonds are results from either Kraus et al. (2016), Wöllert & Brandner (2015), or Furlan et al. (2017), and red squares are measures from DR2 and DR3 of Gaia. The blue lines indicate the best-fit linear solution to the speckle data from our program.

coming years, KOI-270 = Kepler-449 and KOI-1613 = Kepler-907. Having secured further observations of both systems, we discuss each below. Up through Gaia DR3, there have not been separate Gaia positions given for the primary and secondary stars, owing to the relatively small separation between the two stars in both cases.

1. Kepler-449 (KOI-270, TIC 270779644). This double hosts two planets[12] where both have radii less than two Earth radii and are situated within 0.2 au of the host star. The primary star is estimated to have an effective temperature of approximately 5550 K and a radius of 1.4 $R_{\odot}$. A slightly subsolar metallicity has been measured for these stars, and the magnitude difference between the stellar companions is approximately half a magnitude. In Colton et al. (2021), the system was reported as a probable-CPM pair based on observations through 2017. The observations reported here allow us to extend the time baseline of the relative astrometry by five years, and, using the same criteria as in Colton et al. (2021), we conclude that the system is now firmly established as a CPM pair. Figure 13(a) shows the relative motion over time; there appears to be little deviation from linear motion at the present time, though the trend toward a decreasing separation consistent with an edge-on orbit is also confirmed. We also note that there are astrometric measures in the literature from both Adams et al. (2012) and Kraus et al. (2016); the former, based on adaptive optics images taken at the Palomar Hale Telescope, do not have uncertainty estimates, but the wide discrepancy between the separations obtained at the two contemporaneous observations in two filters argues for exclusion from an astrometric analysis. The data from Kraus et al. (2016) is again adaptive optics data, but from the Keck II telescope; those authors report a linear uncertainty in their measures of ∼1.5 mas, comparable to what we report here for the ARC telescope. Although we use only our own speckle data to derive the relative motion of the system in our analysis here, we note that the Kraus measure is consistent with our results, as shown in Figure 13(a).
2. Kepler-907 (KOI-1613, TIC 120576846). This F5V system hosts a single confirmed exoplanet and two planetary candidates. The confirmed planet has a radius of 1.31 $R_{\oplus}$ and a semimajor axis of 0.11 au. The two planetary candidates are both farther from the host star and smaller. The secondary star has a magnitude difference of 1.4 relative to the primary; thus it is most likely a star much like the Sun, perhaps just slightly later in spectral type, G3 or G4. Several observations besides those of our program are reported in the literature due to Law et al. (2014), Wang et al. (2015), Teske et al. (2015), and Kraus et al. (2016). (The speckle measurements of Teske et al. (2015) and Furlan et al. (2017) were superseded by the more carefully calibrated astrometry of Colton et al. (2021) for the same observations.) However, with the exception of the Kraus et al. (2016) measures, the astrometry of these other observations is again not as precise. Fitting our speckle data to a line (Figure 13(b)) results in large residuals in this case, much larger than the typical measurement precision; the reason is that the APO points deviate significantly from the line fit to the values from previous observations. A parabolic fit (also shown in Figure 13(b)) gives much better results, indicating possible

[12] https://exofop.ipac.caltech.edu

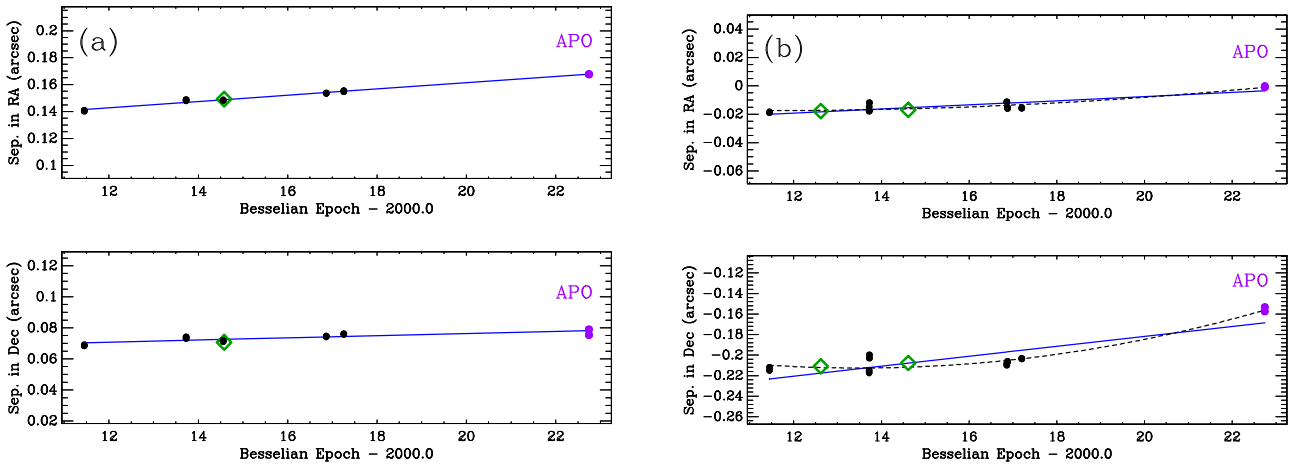

Figure 13. Motion of the stellar secondary relative to the primary over time for (a) Kepler-449, and (b) Kepler-907 (see Section 7.2). In both plots, the filled circles represent observations taken earlier in our program and reported in Colton et al. (2021), the purple filled circles on the right marked "APO" indicate the new data appearing in Table 3, and green diamonds are results from Kraus et al. (2016). The blue lines indicate the best-fit linear solution to the speckle data on our program, and for Kepler-907, the dashed curves indicate the best-fit parabolic solution.

detection of orbital motion. This suggestion will have to be confirmed with future observations, but is nonetheless a tantalizing example of how well-calibrated, long-term astrometry can provide information regarding the status of the Kepler binaries.

8. Conclusions

We have presented results from the first year of operation of DSSI on the ARC 3.5 m telescope at APO, consisting of relative astrometry and photometry for 40 binary star systems. An updated description of the instrument in its current configuration at APO, including addition of an internal slit mask for plate scale calibration, is also included. Combining all results from the first year of operation, including additional results not presented in Table 3, we find an astrometric precision of 2.06 ± 0.11 mas, and a photometric precision of 0.14 ± 0.04 mag. These are consistent with previously reported values for DSSI at WIYN and the LDT.

Using results presented here, along with values from the literature, we also provide revised orbital fits to two systems. In addition, we present updated dispositions on five KOIs previously reported in Colton et al. (2021) for which we have confirmed their status as CPM pairs. For the CPM pair candidate KOI-1613, our new observations indicate an acceleration indicative of orbital motion.

Acknowledgments

We thank Dan Gentile from National Aperture for his help on the slit mask. We also thank the APO staff for all their help with commissioning DSSI at APO. J.W.D. gratefully acknowledges funding from the NASA-NSF Exoplanet Observational Research (NN-EXPLORE) program through JPL RSAs 1560091 and 1569072. E.P.H. acknowledges funding from NSF grants AST-1909560 and AST-2206099. S.R.M. acknowledges funding from a Cottrell Singular Exceptional Endeavors of Discover (SEED) Award from The Research Corporation, as well as a subaward from NASA ADAP Award 80NSSC21K0631 (Veselin Kostov, Principal Investigator) to the SETI Institute.

This research has made use of the Washington Double Star Catalog maintained at the U.S. Naval Observatory, as well as the SIMBAD database, operated at CDS, Strasbourg, France. This work also made use of the Hipparcos Catalogue.

This research has made use of the Exoplanet Follow-up Observation Program (ExoFOP; NExScI 2022) website, which is operated by the California Institute of Technology, under contract with the National Aeronautics and Space Administration under the Exoplanet Exploration Program.

This work presents results from the European Space Agency (ESA) space mission Gaia. Gaia data are being processed by the Gaia Data Processing and Analysis Consortium (DPAC). Funding for the DPAC is provided by national institutions, in particular the institutions participating in the Gaia MultiLateral Agreement (MLA). The Gaia mission website is https://www.cosmos.esa.int/gaia. The Gaia archive website is https://archives.esac.esa.int/gaia.

ORCID iDs

James W. Davidson, Jr. https://orcid.org/0009-0007-1284-7240
Elliott P. Horch https://orcid.org/0000-0003-2159-1463
Steven R. Majewski https://orcid.org/0000-0003-2025-3147
Torrie Sutherland https://orcid.org/0009-0007-4277-0360
D. Xavier Lesley https://orcid.org/0009-0000-5136-6924
Richard A. Pellegrino https://orcid.org/0009-0009-9894-3114
Jonathan P. Leonard https://orcid.org/0000-0002-0353-7060
John C. Wilson https://orcid.org/0000-0001-7828-7257
Nancy J. Chanover https://orcid.org/0000-0002-9984-4670
Todd J. Henry https://orcid.org/0000-0002-9061-2865
Devin McDonald https://orcid.org/0000-0002-9448-6261
Riley A. DeColibus https://orcid.org/0000-0002-1647-2358
Candace Gray https://orcid.org/0000-0003-2871-0779
Amanda Townsend https://orcid.org/0000-0002-6377-4869

References

Adams, E. R., Ciardi, D. R., Dupree, A. K., et al. 2012, AJ, 144, 42
Clark, C. A., van Belle, G. T., Horch, E. P., et al. 2020, Proc. SPIE, 11446, 114462A
Clark, C. A., van Belle, G. T., Horch, E. P., et al. 2022, AJ, 164, 33

Colton, N. M., Horch, E. P., Everett, M. E., et al. 2021, AJ, 161, 21
Crossfield, I. J. M., Ciardi, D. R., Petigura, E. A., et al. 2016, ApJS, 226, 7
Docobo, J. A., & Andrade, M. 2013, MNRAS, 428, 321
Furlan, E., Ciardi, D. R., Everett, M. E., et al. 2017, AJ, 153, 71
Hartkopf, W. I., & Mason, B. D. 2014, IAU Double Star Inf. Circ., 184, 1
Hartkopf, W. I., Mason, B. D., & McAlister, H. A. 1996, AJ, 111, 370
Hartkopf, W. I., Mason, B. D., & Worley, C. E. 2001a, AJ, 122, 3472
Hartkopf, W. I., McAlister, H. A., & Mason, B. D. 2001b, AJ, 122, 3480
Henry, T., Casetti-Dinescu, D., Horch, E., et al. 2022, AAS Meeting Abstracts, 54, 305.15
Horch, E. P., Broderick, K. G., Casetti-Dinescu, D. I., et al. 2021, AJ, 161, 295
Horch, E. P., Casetti-Dinescu, D. I., Camarata, M. A., et al. 2017, AJ, 153, 212
Horch, E. P., Dinescu, D. I., Girard, T. M., et al. 1996, AJ, 111, 1681
Horch, E. P., Gomez, S. C., Sherry, W. H., et al. 2011a, AJ, 141, 45
Horch, E. P., Howell, S. B., Everett, M. E., & Ciardi, D. R. 2012, AJ, 144, 165
Horch, E. P., Howell, S. B., Everett, M. E., & Ciardi, D. R. 2014, ApJ, 795, 60
Horch, E. P., Meyer, R. D., & van Altena, W. F. 2004, AJ, 127, 1727
Horch, E. P., van Altena, W. F., Cyr, W. M., Jr., et al. 2008, AJ, 136, 312
Horch, E. P., van Altena, W. F., Howell, S. B., Sherry, W. H., & Ciardi, D. R. 2011b, AJ, 141, 180
Horch, E. P., van Belle, G. T., Davidson, J. W., Jr., et al. 2015, AJ, 150, 151
Horch, E. P., Veillette, D. R., Baena Gallé, R., et al. 2009, AJ, 137, 5057
Izmailov, I. S. 2019, AstL, 45, 30
Kostov, V. B., Schlieder, J. E., Barclay, T., et al. 2019, AJ, 158, 32
Kraus, A. L., Ireland, M. J., Huber, D., Mann, A. W., & Dupuy, T. J. 2016, AJ, 152, 8
Law, N. M., Morton, T., Baranec, C., et al. 2014, ApJ, 791, 35
Lohmann, A. W., Weigelt, G., & Wirnitzer, B. 1983, ApOpt, 22, 4028
MacKnight, M., & Horch, E. P. 2004, AAS Meeting Abstracts, 204, 07.19
Mann, A. W., Dupuy, T., Kraus, A. L., et al. 2019, ApJ, 871, 63
Mason, B. D., Douglass, G. G., & Hartkopf, W. I. 1999, AJ, 117, 1023
Mason, B. D., Wycoff, G. L., Hartkopf, W. I., Douglass, G. G., & Worley, C. E. 2001, AJ, 122, 3466
Mayo, A. W., Vanderburg, A., Latham, D. W., et al. 2018, AJ, 155, 136
Meng, J., Aitken, G. J. M., Hege, E. K., & Morgan, J. S. 1990, JOSAA, 7, 1243
Muterspaugh, M. W., Hartkopf, W. I., Lane, B. F., et al. 2010a, AJ, 140, 1623
Muterspaugh, M. W., Lane, B. F., Fekel, F. C., et al. 2008, AJ, 135, 766
Muterspaugh, M. W., Lane, B. F., Kulkarni, S. R., et al. 2010b, AJ, 140, 1657
NExScI 2022, Exoplanet Follow-up Observing Program Web Service, IPAC, doi:10.26134/EXOFOP5
Prieur, J. L., Scardia, M., Pansecchi, L., Argyle, R. W., & Sala, M. 2010, MNRAS, 407, 1913
Scott, N. J., Howell, S. B., Gnilka, C. L., et al. 2021, FrASS, 8, 138
Scott, N. J., Howell, S. B., Horch, E. P., & Everett, M. E. 2018, PASP, 130, 054502
Teske, J. K., Everett, M. E., Hirsch, L., et al. 2015, AJ, 150, 144
Wang, J., Fischer, D. A., Xie, J.-W., & Ciardi, D. R. 2015, ApJ, 813, 130
Wenger, M., Ochsenbein, F., Egret, D., et al. 2000, A&AS, 143, 9
Wöllert, M., & Brandner, W. 2015, A&A, 579, A129